
Mechanical behaviour and high strain rate deformation of stainless steel 316L processed by selective laser melting

Travis J. Kneen and Christopher Barrett

Advanced Manufacturing Research Center,
Youngstown State University,
One University Plaza, Youngstown, OH 44555, USA
Email: tkneen@u.rochester.edu
Email: cbarrett@student.yzu.edu

Guha P. Manogharan

Department of Mechanical Engineering,
Pennsylvania State University,
232 Reber Bldg, University Park, PA 16802, USA
Email: gum53@psu.edu

Patrick R. Carlson and Jason Dimon

North Star Imaging,
19875 S. Diamond Lake Rd., Rogers, MN 55374, USA
Email: pcarlson@4nsi.com
Email: jdimon@4nsi.com

Brett P. Conner*

Advanced Manufacturing Research Center,
Youngstown State University,
One University Plaza, Youngstown, OH 44555, USA
Email: bpconner@ysu.edu
*Corresponding author

Abstract: With growing interest in metal additive manufacturing (AM) for aerospace and defence applications, it is important to understand the influence of processing conditions on high strain rate behaviour. This paper presents research on as-built stainless steel 316L AM parts processed using laser powder bed fusion (L-PBF) also referred to as selective laser melting (SLM). Two sets of varied process parameters were examined as well as different build orientations. Laser scan speed and point-to-point distance are shown to have influenced the high strain rate mechanical properties of 316L AM parts. Additionally, both wrought and SLM produced 316L showed strain rate sensitivity (hardening) at strain rates of 10^3 s^{-1} , but this effect was more pronounced in the wrought material. Findings from this study can be used to determine appropriate part orientations and AM process parameters and their influence on the high strain rate behaviour and impact performance of L-PBF AM parts.

Keywords: high strain rate behaviour; additive manufacturing; selective laser melting; SLM; SS 316L; microstructure; process parameters; Charpy tests; split-Hopkinson pressure bar; SHPB.

Reference to this paper should be made as follows: Kneen, T.J., Barrett, C., Manogharan, G.P., Carlson, P.R., Dimon, J. and Conner, B.P. (2020) 'Mechanical behaviour and high strain rate deformation of stainless steel 316L processed by selective laser melting', *Int. J. Rapid Manufacturing*, Vol. 9, No. 1, pp.84-103.

Biographical notes: Travis J. Kneen is a Research Inquiry Analyst at the Defense Systems Information Analysis Center (DSIAC). He holds an MS in Mechanical Engineering from Youngstown State University as well as a BS in Physics and Astronomy from the University of Rochester. His graduate research focused on the mechanical properties of additively manufactured stainless steel 316L.

Christopher Barrett is a Doctoral candidate in the Materials Science and Engineering Program at Youngstown State University. He holds a Master's degree from the University of Colorado Colorado Springs in Chemistry focusing on Environmental Analytical Chemistry, and a Bachelor's degree from Bob Jones University in Chemistry with a minor in Mathematics. He has extensive experience in the additive manufacturing field working for such companies as America Makes and Universal Technology Corporation, and operating numerous commercially available additive manufacturing printers.

Guha P. Manogharan is an Assistant Professor in the Mechanical Engineering Department at Penn State University. He is the leader of the Systems for Hybrid-Additive Process Engineering (SHAPE) lab and his research interests are in the area of material development and characterisation in hybrid and additive manufacturing (AM), including 3D sand-printing, biomedical applications, CNC and non-traditional machining and design optimisation for AM. His primary contribution to AM to date is developing hybrid additive manufacturing methods to seamlessly integrate traditional processes with AM, with a focus on experimental identification of quantitative relationships between design, processing conditions, applications and final part qualification.

Patrick R. Carlson is the Technical Manager for North Star Imaging. He holds a Diploma in Aerospace Non-Destructive Testing from Ridgewater College. He has over 20 years of experience in manufacturing quality control and non-destructive testing.

Jason Dimon is the North East Technical Sales Manager for North Star Imaging. He holds degrees from North Hennepin Community College and Anoka-Ramsey Community College. He has over ten years of experience in supply chain technologies and non-destructive testing technologies.

Brett P. Conner is the Director of the Advanced Manufacturing Research Center and an Associate Professor of Manufacturing Engineering at Youngstown State University. He is also a Co-Founder and Chief Technology Officer at Freshmade3D. He has research interests related to additive manufacturing including multi-material systems, functional graded materials, shock and energy absorption applications, effects of AM defects, qualification approaches, and economics. He received his Bachelor's degree from the University of Missouri in Physics and Masters and Doctorate from MIT in materials science and engineering.

1 Introduction

Additive manufacturing (AM) refers to manufacturing processes that deposit or fuse material together in a layer-by-layer approach until a 3D part is completely fabricated. AM and other direct digital manufacturing processes are considered the driving forces of a ‘third industrial revolution’ (Gu, 2015). With the ever-growing capabilities of AM technologies and feasible material systems in recent years, the ability to create functional parts has become the focus of experimental research and new industrial applications. AM is unique from traditional manufacturing in its ability to manufacture custom, complex designs at lower material and tooling costs without the need for jigs and fixtures enabling economic advantages over conventional manufacturing (Conner et al., 2014; Manogharan et al., 2018). One area of significant interest is the use of AM for structures that must withstand high strain rate loading such as projectile impact (ARL Public Affairs, 2018; Gray et al., 2017; Johnson et al., 2015).

According to ISO/ASTM52900-15 (ISO/ASTM, 2015), powder bed fusion (PBF) is “an additive manufacturing process in which thermal energy selectively fuses regions of a powder bed” based on CAD information of the part design. Selective laser melting (SLM) also known as laser powder bed fusion (L-PBF) is a PBF process that uses a laser source in an inert atmosphere of nitrogen or argon to fuse particles onto a substrate. This is accomplished by selectively melting a spread layer of metal or polymer powder above its melting temperature using the laser scan (Gu, 2015). Once the laser selectively melts a layer, another layer is spread as the powder bed is lowered by the layer thickness (or slice height). This process is repeated until the final geometry is created.

SLM is of particular interest to the aerospace, medical, automotive, electronic, and tooling industries (Cherry et al., 2015; Spierings and Levy, 2009; Stwora and Skrabalak, 2013; Trelewicz et al., 2016; Yadroitsev and Smurov, 2011). It offers the ability to manufacture a near-net shape part while eliminating tooling and lowering material costs with the flexibility to process multiple geometries within the same build. Of particular importance is the ability to manufacture lattice structures such as non-stochastic foams and lattices (Tsopanos et al., 2010) within part geometries for biomedical implants (Stwora and Skrabalak, 2013) and weight reduction in aerospace applications (Tsopanos et al., 2010). Since AM requires a CAD file and is sliced prior to manufacturing, there has been an increased focus on topological optimisation due to greater freedom of design such that AM parts can be closer to an optimum design that cannot be achieved using traditional manufacturing (Brackett et al., 2011). L-PBF materials that have been studied include cobalt-chromium alloys (Yadroitsev and Smurov, 2010; Zhou et al., 2015), copper compounds (Yadroitsev and Smurov, 2010), 24 karat gold (Khan and Dickens, 2014), aluminium and aluminium alloys (Romano et al., 2017; Zhou et al., 2018), titanium alloys (Gong et al., 2014; Qiu et al., 2013, 2015; Santos et al., 2004; Simonelli et al., 2014; Vrancken, et al., 2014a, 2014b), nickel-base superalloys (Barrett et al., 2018; Yadroitsev et al., 2007), tool steels (Rombouts et al., 2006; Simchi, 2006; Stwora and Skrabalak, 2013), iron powders (Kempen et al., 2011; Kruth et al., 2004; Rombouts et al., 2006; Simchi, 2006; Simchi et al., 2003), and stainless steel alloys (Badrossamay and Childs, 2007; Brown, 2014; Ma et al., 2015; Yadroitsev and Smurov, 2011; Yasa and Kruth, 2011), with growing research efforts expanding feasible material systems including metal matrix composites (Farayibi and Abioye, 2019). Of note to this work are

the prior investigations in stainless steel 316L in metal AM (Badrossamay and Childs, 2007; Blandford et al., 2007; Badrossamay and Childs, 2007; Blandford et al., 2007; Chen et al., 2018; Cherry et al., 2015; Davies et al., 2018; Ganesh et al., 2014; Gray et al., 2017; Keicher et al., 1996; Kong et al., 2019; Król et al., 2013; Li et al., 2010; Majumdar et al., 2005; Mindt et al., 2016; Riemer et al., 2014; Simchi, 2006; Spierings and Levy, 2009; Tang et al., 2019; Tolosa et al., 2010; Trelewicz et al., 2016; Tsopanos et al., 2010; Yadroitsev and Smurov, 2011; Yakout et al., 2019; Yasa and Kruth, 2011). These studies employ a range of powder size and morphology, AM technologies, and AM process parameters which can be attributed to a lack of standard processing practices that specifies feedstock, machine configuration, processing conditions and post-build operations. New standards are currently being developed and published for AM [America Makes & ANSI Additive Manufacturing Standardization Collaborative (AMSC), 2017; Monzon et al., 2015].

Typical AM process parameters that have been studied include: laser power (P), laser scan speed or velocity (v), laser scan or hatch spacing (h), layer thickness (w), laser point-to-point distance (d), laser exposure time (t), and scan strategy. Experiments often rely on a trial and error approach based on specimen density, melt pool morphology, final part mechanical strengths, and microstructure to determine optimal parameters for the desired material and part geometry (Badrossamay and Childs, 2007; Cherry et al., 2015; Qiu et al., 2013, 2015; Tolosa et al., 2010; Yadroitsev and Smurov, 2010, 2011; Yasa and Kruth, 2011; Zhou et al., 2015). Laser power density and layer thickness have been proposed as the primary factors that influence part density and mechanical properties which are determined by melt pool and resulting microstructure characteristics (Gu, 2015; Simchi, 2006).

It is important to note that there is no standard currently available for Split-Hopkinson pressure bars (SHPB) experiments, similar to the lack of standardisation of AM (Chen and Song, 2010). Winter et al. (2014) fabricated 316L cellular structures and performed impact testing using a gas-gun-driven flyer at rates varying from 3×10^5 and 7×10^5 s⁻¹. Similar work compared direct energy deposition (DED) manufactured SS 316L and DED heat treated parts to wrought plate (Gray et al., 2015). However, there have been exhaustive investigations into powder metallurgy (PM) SS 316L specimens. High strain rate behaviour of SS 316L is critical since it is widely used in aerospace, automobile, defence, and nuclear applications (Lee et al., 2006, 2012; Lee and Chiu, 2006) where parts may be subjected to high speed collisions and/or explosions (Lee et al., 2012). Lee et al. (2006) compared the compressive properties of three relative sintered densities (83, 88, and 93%) of SS 316L under different quasi-static (10^{-3} to 10^{-1} s⁻¹) and dynamic strain rates (3×10^3 to 9×10^3 s⁻¹). It was determined that the mechanical behaviour of 316L is sensitive to both strain rate and sintered density. Lee et al. (2006) further examined the strain rate effects on sintered 316L specimens (96% dense) using quasi-static and dynamic strain rates. It was determined that at increasing strain rate, the yield strength increased while the strength and work-hardening coefficients decreased. It was also shown that at strain rates greater than 5.6×10^3 s⁻¹, fracture occurred due to plastic instability and that the specimens failed in a ductile mode. Another study performed by Lee et al. (2012) examined the high temperature effects on sintered 316L samples at different strain rates (1×10^5 to 5×10^5 s⁻¹) (Lee et al., 2012). Similar to the prior study (Lee et al., 2006), it was found that the yield strength and work coefficient increased with

increasing strain rate, but decreased with increasing temperature which implies sensitivity of high strain rate behaviour to correlation between temperature and strain rate.

With the growing desire to fabricate functional metal AM parts, there is a clear need to explore the influence of process parameters on resulting mechanical properties. Although prior studies on 316L AM exists, they are only focused on process optimisation and quasi-static mechanical testing. Current research on high strain rate testing of AM materials is limited since it does not account for the influence of build orientation. For instance, an understanding of optimal build orientation of the part for maximum impact resistance will enable optimal reorientation of the part impact surface in AM process planning. The objective of this work is to compare the high strain rate mechanical behaviour of wrought 316L versus additively manufactured L-PBF 316L at two distinctly varied AM processing conditions and also examine the effect of AM build orientations. This experimental research will evaluate the feasibility to fabricate metal AM parts with comparable strengths to wrought material.

2 Experimental methods

Stainless steel 316L test specimens using two different sets of process parameters were printed via L-PBF processing using a Renishaw AM 250 machine as shown in Table 1. Unlike other SLM processes, the AM 250 fires the laser at a spot for a fixed duration then moves to the next spot along a track (i.e., pulsed laser source). This differs from commonly reported L-PBF processes where the laser melt pool is continuously moving along the track. Scanning speed, v is defined as the speed of laser scan, or raster, across the powder bed [Figure 1(a)]. Exposure time, t , is defined as the length of time the laser spot remains at a single point [Figure 1(b)]. Laser point-to-point distance (sometimes referred to as point difference), d , is defined as the distance between two subsequent laser spots [Figure 1(c)]. The rationale behind selecting these two varied sets of process parameters is to induce distinctly different melting and solidification rates that can be eventually coupled with computational modelling tools.

Table 1 Two sets of printer process parameters

<i>Parameter set</i>	<i>Laser power P (W)</i>	<i>Scanning speed v (mm/s)</i>	<i>Exposure time t (μs)</i>	<i>Laser point-to-point distance d (μm)</i>	<i>Laser spot diameter (μm)</i>
1	200	590	110	65	75
2	200	550	90	50	

Particle distribution was examined using a Cilas 1190 laser particle size analyser. The examination was performed in ‘wet’ mode in which powder is dispersed in water and the analyser utilises three lasers to measure particles within the range of 0.04–2,500 μ m (Cilas, 2018). The powder was examined using both x-ray fluorescence (XRF) and x-ray diffraction (XRD). The XRF analysis was performed in metals mode in a S2 Ranger fluorescence spectrometer equipped with a Si-Li detector and Rh and Pd target. The XRD analysis was conducted using a Bruker-Nonius D8 Advance Powder Diffractor, which is equipped with a VANTEC-1 detector for fast simultaneous recording of XRD patterns over a wide 2θ range.

Figure 1 (a) Scanning speed (b) Exposure time, and (c) Point difference (see online version for colours)

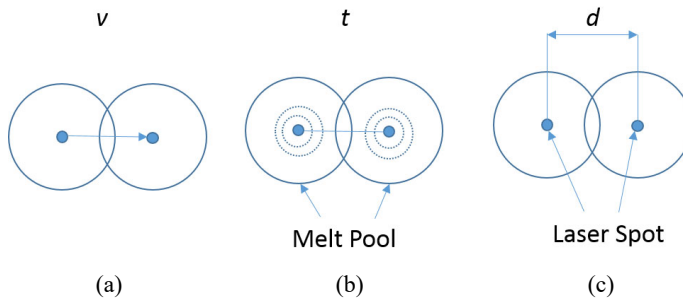


Figure 2 (a) ZX- (b) XZ- and (c) XY-build orientations of L-PBF specimens (see online version for colours)

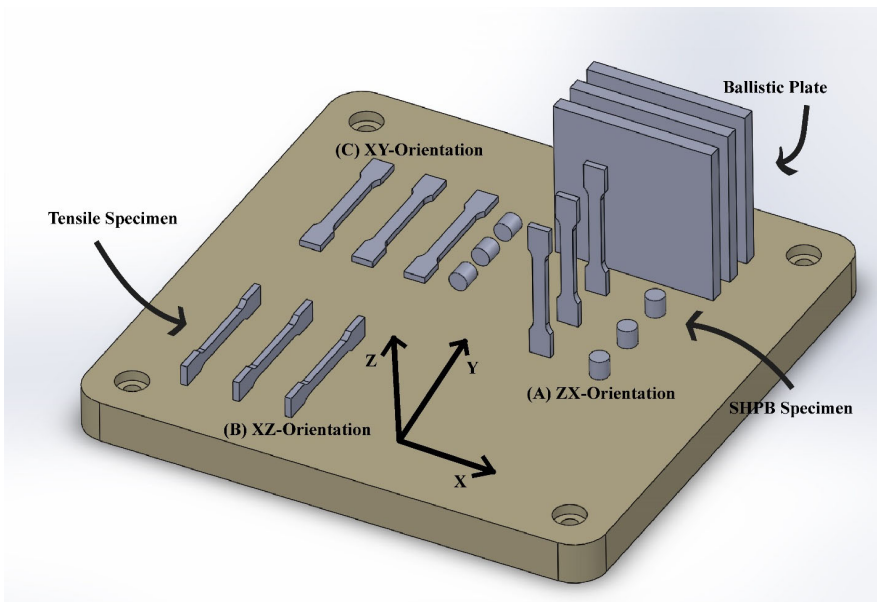
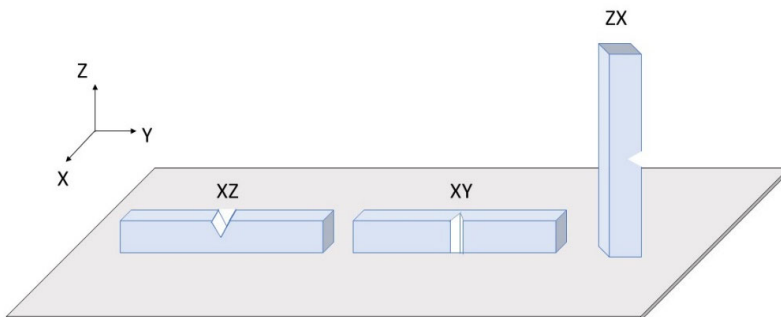


Figure 3 Notch orientations for Charpy specimens are shown here (see online version for colours)



Parts were printed in three orientations: *XY* (flat), *ZX* (vertical), *XZ* (on-edge) as shown in Figure 2. These are labelled according to ISO/ASTM 52900 (ISO/ASTM, 2015), where the largest axis is listed first and the second largest axis is listed second. The notch orientations of the Charpy specimens are shown in Figure 3.

In order to isolate the effects of orientation and laser parameters from post-processing, the parts were evaluated in the as-built state. The parts were removed from the steel build plate using a band saw and were not subjected to stress-relief annealing or any heat treatment.

Mechanical testing was performed to compare additively manufactured parts to wrought specimens in both quasi-static and dynamic strain rates using ASTM testing conditions specified in Table 2. Samples from each orientation were made for tensile and Charpy testing ($n = 5$) and the split Hopkinson testing ($n = 12$). Dimensions of the cylindrical SHPB specimens were a length of 9.1 mm and diameter of 8.8 mm, printed with supports. The supports were subsequent removed mechanically.

The Rockwell D and Brinell hardness tests were performed using a Buehler Macromet 3 and Tinius Olsen Air-O-Brinell, respectively. These tests were performed on flat plates in the *ZX* orientation designed for use as ballistic testing specimens for a separate project. Five indentations ($n = 5$) were performed on a large area face of each plate.

Quasi-static tensile testing was conducted in an Instron 4206 universal testing machine with a 150 kN load cell with a resolution of $\pm 0.25\%$ of full load using an Instron 5500R mounting. Data was recorded using both the BlueHill 3 software and using a P3 strain indicator and a quarter-Wheatstone bridge circuit. High strain-rate compression tests were performed using an REL SHPB, controlled using the software PicoScope, and recorded using the software SURE-Pulse. Impact tests were performed using Charpy V-notch specimens prepared by electrical discharge machining (EDM) and a Tinius Olsen model IT 406 test rig.

Table 2 Mechanical tests based on ASTM Standards

<i>Test</i>	<i>ASTM standard</i>	<i>Specimen type</i>	<i>Testing conditions</i>	<i>Experimental results</i>
Hardness (Rockwell D, Brinell)	E18-15 (American Society for Testing Materials, 2015) and E10-15a (ASTM International, 2015)	Polished 6.35 mm (0.25 in) thick plate printed in <i>ZX</i>	Rockwell D: diamond tip with 100 kg major load Brinell: 100 mm tungsten carbide spherical indenter with 3000 kg load for 20 seconds	Hardness numbers (HRD, HB)
Tensile	E8/8M (ASTM International, 2009a), and A370 (ASTM International, 2009b)	Sub-sized rectangular flat-bar standard (6 mm wide) printed in <i>XY</i> and <i>ZX</i> for both parameters sets and also in <i>XZ</i> for parameter set 2.	Loaded at a strain rate of 28.575 1/s 6.35 (according to the reduced cross-section) and data recorded using strain gauges	Elastic modulus (E), ultimate tensile strength (UTS), 0.2% yield strength (YS), reduction of area (RA)

Table 2 Mechanical tests based on ASTM Standards (continued)

<i>Test</i>	<i>ASTM standard</i>	<i>Specimen type</i>	<i>Testing conditions</i>	<i>Experimental results</i>
Charpy V-Notch	A370 (ASTM International, 2009b), and E23-12c (ASTM International, 2012)	55 × 10 × 10 mm rectangles with 0.25 mm EDM notch at 45° printed in <i>XY</i> and <i>ZX</i> for both parameters sets and also in <i>XZ</i> for parameter set 2.	Specimens struck by 22.68 kg (50 lb) hammer from 1.829 m (6 ft) for 400.75 J (300 ft-lb)	Energy absorbed
Split-Hopkinson pressure bar compression testing	N/A	Cylinders with height of 9.1 mm and diameter of 8.8 mm printed in <i>XY</i> and <i>ZX</i>	Using gas gun set at 100 psi for an average strain rate in the 10 ³ s ⁻¹ range	0.2% yield strength (YS), ultimate compressive strength (UCS)

Polished and etched surfaces were analysed via light microscopy (LM) using a Zeiss-Axiophot LM with Pixielink-model PL A662 CCD camera for porosity and grain structure examinations. Scanning electron microscopy (SEM) was conducted using a JEOL JSM-7600F field emission SEM (FE SEM) and a JEOL JSM-IT300LV variable pressure SEM (VP SEM). The powder, etched surfaces, and fracture surfaces were imaged in the secondary electron mode of the SEM. Samples were polished down to a 0.5 µm finish and chemically etched via immersion in Vilella's reagent (1 g picric acid, 5 mL hydrochloric acid, 100 mL ethyl alcohol) for 60 minutes.

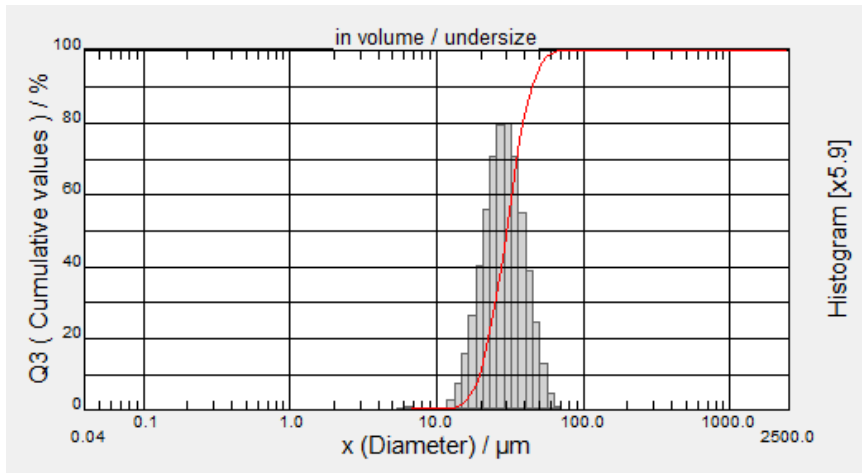
Computerised tomography (CT) was used to check for porosity within the printed parts and analysed using EfXct software. A North Star Imaging NSI X5000 DR/CT System was used for the CT characterisation and a 225kv micro focus cone beam coupled with a flat panel detector was chosen for the data collection. The samples were maximised across the flat panel in order to achieve high image quality. The greater the geometric magnification of the product, the greater the spatial resolution or the ability to resolve smaller detail. The data collected is turned into 3-dimensional voxel data, or cubes that compose the volume of data, the CT scan.

3 Results and discussion

Results from powder, mechanical testing, microstructural analyses, and CT scans are presented in this section.

3.1 Powder analysis

Based on the particle distribution methodology presented in Section 2, the 10th, 50th, and 90th percentiles were determined to be approximately 19.51 µm, 29.84 µm, and 44.67 µm, respectively. The measured particle size distribution is shown in Figure 4. It was found that the powder distribution between the 10th and 90th percentiles were within range, which followed the expected distribution based on the 15+/-45 Renishaw range.

Figure 4 Particle size distribution (see online version for colours)

Quantitative analysis of the 316L powder prior to AM processing using XRF was compared to ASTM A240 standards (ASTM International, 2011). The chemical composition of the L-PBF 316L powder resulted in 67.5% Fe, 17.9% Cr, 10.3% Ni, 2.22% Mo, and 1.36% Mn, which are within the requirements of ASTM A240. There were alloying elements that are listed in ASTM A240 that were not found in the XRF analysis including N, C, and S because they were below the detection limit, as well as elements that were found not listed in the standard including Cu, V, and Nb. However, these alloying elements are little more than trace amounts that should not affect the overall chemical composition. XRD analysis of the powder yielded a cubic, face-centred (Fm-3m) crystal structure with a unit cell length of approximately 3.618 angstroms (Å), which is expected from stainless steel.

3.2 Hardness testing

As shown in Table 3, L-PBF samples produced using process parameters 2 showed comparable results to wrought specimens.

Table 3 Brinell and Rockwell D test results on L-PBF printed 316L with two different process parameter sets and compared to reported wrought results

<i>Process parameter</i>	<i>Brinell (HB)</i>	<i>Rockwell (HRD)</i>	<i>Equivalent tensile (MPa)</i>
1	150.6 ± 7.4	26.6 ± 0.9	521
2	180.4 ± 7.1	30.7 ± 0.9	558–612
<i>Wrought</i>	170	33	579

There was an increase in hardness values in both hardness tests in the case of second parameter set suggesting a possible increase in the density. For continuous L-PBF produced 316L, Tolosa et al. (2010) reported an average of 235 HV, which is equivalent to about 229 HB or 40.5 HRD, while Cherry et al. (2015) reported a similar average value of 225 HV, corresponding to about 220 HB or 39.5 HRD.

3.3 Tensile testing

As shown in Table 4, there is an increase in the elasticity and ultimate strength from the first to second process parameters.

Table 4 Tensile results of AM and Wrought specimens

<i>Specimen group</i>	<i>E (GPa)</i>	<i>UTS (MPa)</i>	<i>σ_y (MPa)</i>	<i>Reduction of area (%)</i>
XY-1	185 ± 39	584 ± 12	486 ± 13	27 ± 9
ZX-1	153 ± 71	441 ± 81	365 ± 79	46 ± 6
XY-2	226 ± 43	604 ± 15	492 ± 17	31 ± 6
ZX-2	206 ± 55	560 ± 7	464 ± 12	46 ± 4
XZ-2	195 ± 14	589 ± 47	427 ± 64	31 ± 6
Wrought	191 ± 22	585 ± 57	260 ± 59	67 ± 2

Each group of specimens, with the exception of *ZX-1*, compare favourably to the wrought samples in terms of elasticity and ultimate strength. However, every specimen group outperformed the wrought in yield strength and exhibited substantially lower ductility as observed from % area reduction. The values are comparable to previously reported laser L-PBF studies in the Senvol database: 150–195 GPa for *E*, 585–686 MPa for UTS, and 45–59% for reduction of area (Database, 2016). *XY-2* data also favourably compares to SLM literature data reported Montero Sistiaga et al. (2016) for as-built 316L from a continuous laser SLM 280 system where UTS was reported near 630 MPa and yield strength of 500 MPa.

3.4 Charpy V-notch

Results from Charpy V-notch tests are shown in Table 5. The first parameter parts were weak by a substantially large amount, most likely due to the high porosity as discussed in Section 3.6. The second parameter specimens were relatively stronger, eclipsing the average value of 56.8 J reported by Tolosa et al. (2010) but slightly lower the values of 90–110 J reported by Ganesh et al. (2014). However, these results compare unfavourably to reported values of traditionally manufactured Charpy V-notch specimens of either ≥ 75 J (Tolosa et al., 2010) or 105 J (Ganesh et al., 2014), except for *ZX* build direction produced using the second set of parameters. In general, the results for *XY* and *ZX* are lower than the as-built SLM 280 parts in Montero Sistiaga et al. (2016) with reported *XY* and *XZ* values from 120 to 130 J but no *ZX* values were measured in Montero Sistiaga et al. (2016). More recent results for as-built SLM 316L can be found in Davies et al. (2018) where *XZ* was reported as 60–62 J which is very similar to the values found here. However, Davies et al. (2018) reported *ZX* as only 22–24 J which is similar to the impact energies from the first set of parameters shown here in Table 5 but is far less than the second set of parameters here.

These as-built toughness results can be compared to literature values for post-processed SLM parts. Charpy specimens produced using an EOS M 270 then post-processed with hot isotatic pressing (HIP) followed by solution annealing were reported in Lou et al. (2018) with values of 130–150 J. The increase in toughness for this combination of HIP plus solution annealing can be expanded by the combination of densification from HIP, recrystallisation from a cellular dendrite structure as found in the

as-built specimens to a larger grain size, and effect of solution strengthening Montero Sistiaga et al. (2016) and Lou et al. (2018).

Table 5 Charpy V-notch results

<i>Specimen group</i>	<i>Energy absorbed (J)</i>
XY-1	29 ± 9
ZX-1	16 ± 5
XY-2	81 ± 9
ZX-2	128 ± 31
XZ-2	58 ± 13

3.5 SHPB compression testing

The experimental results shown in Table 6 represents a similar trend to prior SHPB experiments on non-AM 316L: materials are affected by strain rate such that they exhibit greater ultimate and yield strengths at higher strain rates. The targeted strain rate was 2,000 s⁻¹ however the SHPB system used had inherent variability so actual test strain rate values ranged from 1,838 s⁻¹ to 2,739 s⁻¹. There were only three wrought SHPB tests. For the SLM specimens from parameter set 1, there were 11 valid tests each for the *XY* and *ZX* orientations. However, there were only three valid tests (i.e., tests within 30% of the targeted strain rate of 2,000 s⁻¹) for parameter 2 and they were all in the *ZX* orientation.

Given the limited amount of tests and the scatter associated with the wrought and *ZX* tests, only general observations can be made. Compared to the static tensile testing, considerable strengthening occurred at the higher strain rates. Tensile strengths are similar for all the process methods. However, the wrought material had substantially greater yield strengthening as compared to all AM processes sets and orientations. The recorded maximum and yield strengths here are close to those reported by Lee and Chiu (2006), who conducted SHPB testing of PM samples of relative sintered densities of 316L at 83%, 88%, and 93%. Lee and Chiu noted that the P/M 316L was highly strain rate sensitive and the yield strength increase with increasing strain rates. At a strain rate of 3,000 s⁻¹ they reported fracture stresses of approximately 1,060 MPa for densities of 83% and 88% and fracture stress of 1,076 MPa for 93% dense specimens. They also reported yield strengths for the 83%, 88%, and 93% dense specimens as approximately 375, 395, and 420 MPa, respectively. Comparing measurements and literature values, the greatest increase in yield strength at high strain rate (10³ s⁻¹) was for the wrought plate. The next greatest increased was for the as-built L-PBF material and then followed by the PM specimens in Lee and Chiu (2006).

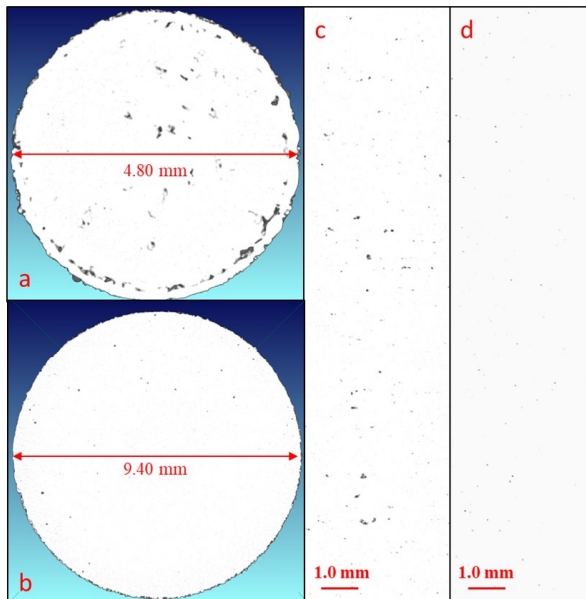
Table 6 SHPB compression testing results

<i>Specimen group</i>	<i>Max strength (MPa)</i>	<i>σ_y (MPa)</i>
XY-1	1,017 ± 44	768 ± 105
ZX-1	1,017 ± 27	776 ± 49
ZX-2	1,046 ± 149	653 ± 193
Wrought	1,202 ± 166	1,020 ± 118

3.6 Microstructural and CT scan analysis

For the CT scanning, the specimen from the first parameter set 1, was smaller in physical size (diameter of 4.80 mm) allowing for more geometric magnification or a smaller voxel size of 10.5 μm . The specimens for parameter set 2 was slightly larger in size (diameter of 9.40 mm) netting a 12 μm data set. The difference of the two scans being 1.5 μm , this was negligible for this study due to the comparison of larger voids. The data sets were both capable of detecting indications in the mid to upper 20 μm range. The porosity, as expected from the mechanical testing results, is greater in the first parameter specimens than those manufactured with the second set of parameters. This can be observed from the CT images in Figure 5. Representative CT scan slice images were acquired and thresholded to convert the images into representative 8 bit binary black and white images. Part densities were then computed using ImageJ by calculating the ratio of the white pixels to the total number of pixels. For the parameter set 1 cylindrical specimen, the image analysis showed a density of 93.4% in the XY plane [Figure 5(a)] and an average density of 96.6% in the ZX plane [Figure 5(c)]. For the parameter set 2 cylindrical specimen, the image analysis showed a marked improvement with a density of 99.7% for the XY plane [Figure 5(b)] and an average density of 99.9% for ZX plane [Figure 5(d)]. The parameter set 1 specimen contained rounded indications and lack of fusion indications in excess of 250 μm . These indications were larger in size as compared to parameter set 2. No lack of fusion indications were found in the parameter set 2 specimen, and it contained far fewer rounded indications as compared to the parameter set 1 specimen. The largest indication seen in the parameter set 2 specimen was a maximum of 145 μm .

Figure 5 CT Scan images for (a) specimen created using parameter set 1 top down (XY Plane) view (4.80mm diameter rod) (b) specimen created using parameter set 2 top down (XY Plane) view (9.40mm diameter rod) (c) specimen from (a) side (ZX Plane) view (d) specimen from (b) side (ZX Plane) view (see online version for colours)



There are a large number of pores in the first parameter specimen in the *ZX* orientation, as identified in Figure 6(a), which is improved in the second parameter specimen shown in Figure 6(b). In both instances, melt pool paths and cross-hatching of laser scans are evident.

Figure 6 (a) Laser parameter set 1 *ZX* orientation specimen light micrograph at 100x
(b) Laser parameter set 2 *ZX* orientation at 100x (see online version for colours)

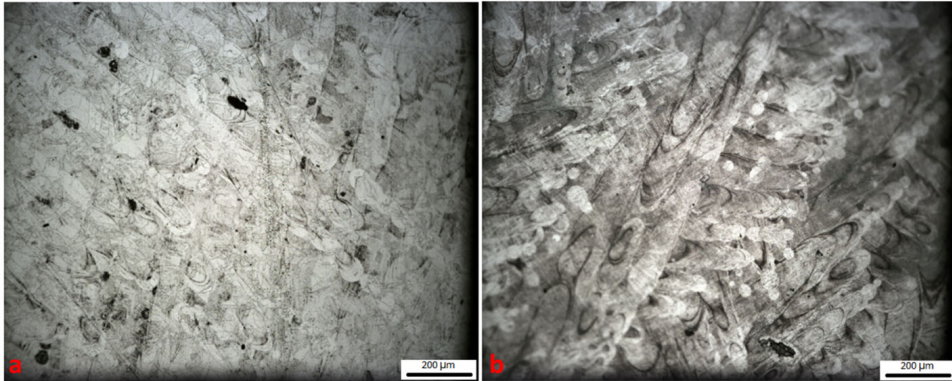
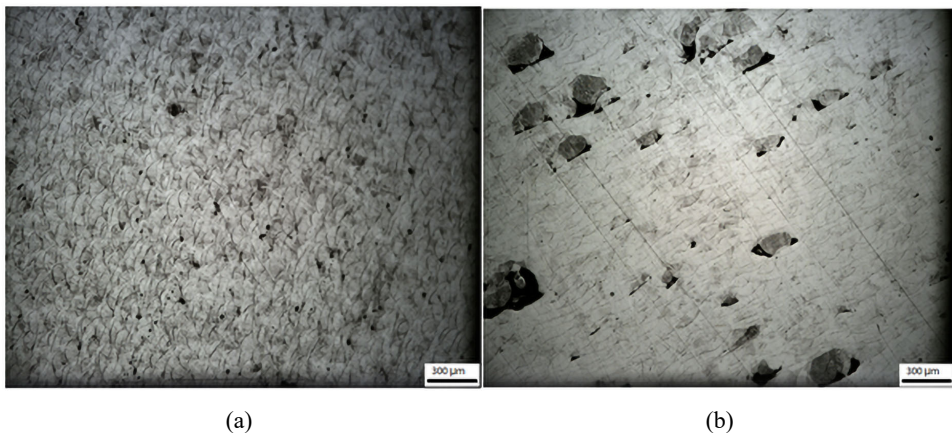


Figure 7 (a) *ZX-1* light micrograph at 50x and (b) *XY-2* light micrograph at 50x



A further examination of the types of defects between the two sets of process parameters is presented in Figure 7. With parameter set 1, there is a large amount of pores associated with the lack of fusion defects (inadequate overlap of the melt pools either laterally or in depth) and micro pores throughout the specimen. As was shown in the CT scan, parameter set 2 improved the overall porosity issue as fewer lack of fusion pores are apparent. However, in Figure 7(b), a region was selected with a significant number of spherical defects. The size of these spheres (~100 to 300 μm) are much greater than the powder size distribution of 15-45 μm . This means these defects are not unfused powder but rather spatter ejected from the melt pool then landing on the part. It is apparent that this spatter is causing significant cavitation around the particle. This could indicate the

pulsed laser AM 250 system could not effectively recoat enough powder around the spatter particle or the spatter landed in the powder bed in advance of the laser beam and reduced the local density of powder available for melting.

Figure 8 (a) Secondary backscatter images taken at 50x on Charpy fracture surfaces: loose particulates from lack of fusion and defect cracks in the first parameter set ZX orientation (b) fewer unmelted powders are seen on the fracture surface from the second parameter set ZX orientation (see online version for colours)

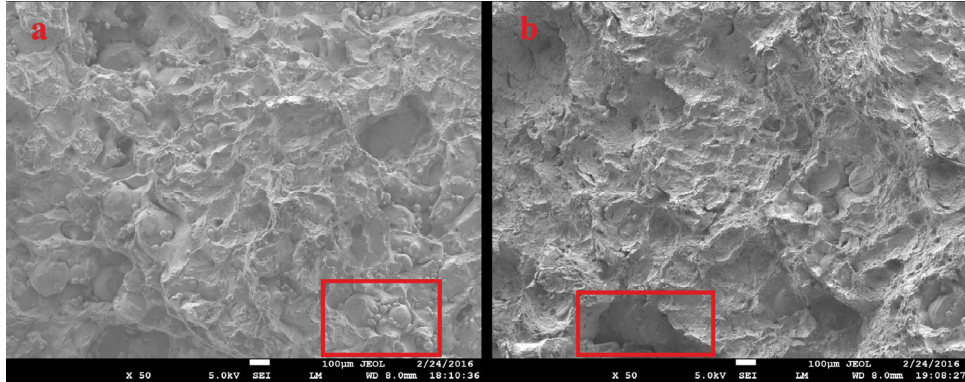
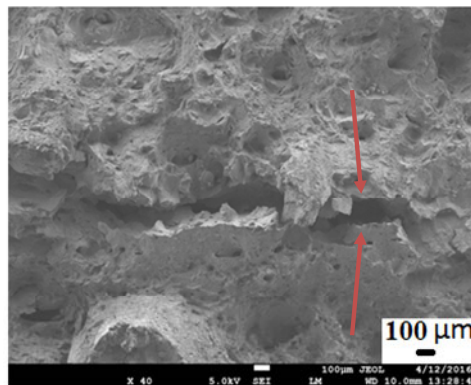


Figure 9 Crack propagation and defects in Charpy fracture surface from parameter set 2 in the XY orientation (see online version for colours)



After undergoing mechanical tests, the fracture surfaces of the median Charpy specimen from each parameter were evaluated using the FE-SEM. Figure 8(a) illustrates the presence of powder that is not fully melted on the fracture surface of a specimen in the ZX orientation from the parameter set 1. Two reasons exist for the unmelted powder. The first is due to lack of fusion defects from lower laser energy density along with higher scan speed. The second reason is lack of fusion around larger spatter particles as unmelted powder can be seen next to larger spatter spheres. During loading conditions, unmelted particles weakens specimens by acting as crack initiation locations as highlighted in Figure 8(a). The parameter set 2 specimens appear relatively denser and fully melted, as shown in Figure 8(b), but some crack initiation sites from L-PBF defects were observed. It should be noted that the fracture surfaces in this study appear to be

almost entirely ductile, which is noted from the dimple-like fracture surfaces shown in Figure 8.

Inspection of the cracks in the fracture surface indicate that lack of fusion served as crack initiation sites. An example is presented in Figure 9, where a large linear void creates a crack front across the image.

4 Conclusions

This work aimed to determine the high strain rate behaviour of as-build stainless steel 316L parts pulsed-laser SLM and examine the effect of orientation for two different sets of SLM process parameters. When relating the AM results of this study to the wrought results and to those from continuous laser L-PBF in the literature, it was determined that overall the first set of SLM processing parameters ($P = 200$ W, $v = 590$ mm/s, $t = 110$ μ s, $d = 65$ μ m) produced unfavourable material properties due to porosity from lack of fusion defects. On the other hand, the second set of processing parameters ($P = 200$ W, $v = 550$ mm/s, $t = 90$ μ s, $d = 50$ μ m) resulted in material properties comparable to both the wrought values and the literature values, especially in the *XY* and *ZX* orientations. The first parameter parts suffered from a large amount of porosity and lack of fusion defects that contained un-melted particles. However, due to the nature of the L-PBF process and the ensuing grain sizes formed by rapid solidification of molten metal, the resulting parts have higher yield strengths, but lower ductility values. The second set of parameters increased the mechanical properties almost across the board, and created parts denser and with fewer defects. Still, even with an increased laser energy density, the fracture surfaces of the Charpy V-notch specimens contained areas where particles were not fully melted. In every test except the Split-Hopkinson, the results proved that the L-PBF parts are affected by both density and print orientation, either due to build layers or particle melting. SHPB showed that the strengths of the L-PBF parts were strain-rate sensitive but not as much as the wrought plate.

This study only explored two limited sets of process parameters on the Renishaw AM250, and for a more meaningful conclusion of the role of process parameters on SLM 316L's high strain-rate behaviour there must be more experimentation with the process parameters. An increase in energy density for parts thicker than tensile bars could increase the density and mechanical properties, while reducing defects.

This work was focused on determining whether AM parts can be used in high strain-rate applications; while initial results are promising additional studies including in-process monitoring and process modelling of pulsed laser based L-PBF systems are required.

Acknowledgements

The authors would like to acknowledge the Youngstown State University Research Council for funding this research. They would also like to acknowledge America Makes and the Innovation Factory managers, Kevin Collier and Rodrigo Enriquez Gutierrez for the use of the Renishaw AM 250. The authors acknowledge Northstar Imaging for the CT scanning images, the YSU Geology Department for the use of the particle analyser, the *YSU Center of Excellence in Materials Science and Engineering* (CEMSE) for use of the

electron microscopes and XRD equipment. The electron microscopes were funded by NSF support DMR #1229129 (FE-SEM) and an Ohio Board of Regents Grant S932-12 (VP-SEM).

References

- America Makes & ANSI Additive Manufacturing Standardization Collaborative (AMSC) (2017) *Standardization Roadmap for Additive Manufacturing*, American National Standards Institute (ANSI)/National Center for Defense Manufacturing and Machining [online] https://www.ansi.org/standards_activities/standards_boards_panels/amsc/Default?menuid=3 (accessed 24 July 2019).
- American Society for Testing Materials (2015) *Standard Test Methods for Rockwell Hardness of Metallic Materials*, No. E18-15, ASTM International [online] <https://market.android.com/details?id=book--dbdjgEACAAJ> (accessed 24 July 2019).
- ARL Public Affairs (2018) *Army Looks to Nature to Improve Body Armor*, Armed with Science, 1 October [online] <https://science.dodlive.mil/2018/10/01/army-looks-to-nature-to-improve-body-armor/> (accessed 24 July 2019).
- ASTM International (2009a) *Standard Test Methods for Tension Testing of Metallic Materials*, No. E8/E8M - 09, ASTM International [online] https://books.google.com/books/about/ASTM_E8_E8M_09_Standard_Test_Methods_for.html?hl=&id=M7aNrgEACAAJ (accessed 24 July 2019).
- ASTM International (2009b) *Standard Test Methods and Definitions for Mechanical Testing of Steel Products*, No. A370-10, ASTM International [online] https://books.google.com/books/about/A370_10_Standard_Test_Methods_and_Defini.html?hl=&id=qScrYAAACAAJ (accessed 24 July 2019).
- ASTM International (2011) *Specification for Chromium and Chromium-Nickel Stainless Steel Plate, Sheet, and Strip for Pressure Vessels and for General Applications*, No. ASTM A240 / A240M, ASTM International [online] https://doi.org/10.1520/a0240_a0240m-11 (accessed 24 July 2019).
- ASTM International (2012) *Standard Test Method for Notched Bar Impact Testing of Metallic Materials*, No. E23-12c, ASTM International [online] <https://market.android.com/details?id=book-uHlpAQAACAAJ> (accessed 24 July 2019).
- ASTM International (2015) *Standard Test Method for Brinell Hardness of Metallic Materials*, No. E10-15a, ASTM International [online] <https://doi.org/10.1520/e0010-14> (accessed 24 July 2019).
- Badrossamay, M. and Childs, T.H.C. (2007) 'Further studies in selective laser melting of stainless and tool steel powders', *International Journal of Machine Tools & Manufacture*, Vol. 47, No. 5, pp.779–784.
- Barrett, C., MacDonald, E., Conner, B. and Persi, F. (2018) 'Micron-level layer-wise surface profilometry to detect porosity defects in powder bed fusion of Inconel 718', *JOM Journal of the Minerals Metals and Materials Society*, Vol. 70, No. 9, pp.1844–1852, Springer US.
- Blandford, R.K., Morton, D.K., Snow, S.D. and Rahl, T.E. (2007) 'Tensile stress-strain results for 304L and 316L stainless steel plate at temperature', *ASME 2007 Pressure Vessels and Piping Conference, American Society of Mechanical Engineers*, pp.617–628.
- Brackett, D., Ashcroft, I. and Hague, R. (2011) 'Topology optimization for additive manufacturing', *Proceedings of the Solid Freeform Fabrication Symposium*, Vol. 1, No. S, pp.348–362, Austin, TX.
- Brown, B. (2014) *Characterization of 304L Stainless Steel by Means of Minimum Input Energy on the Selective Laser Melting Platform*, Master's degree, Missouri University of Science and Technology [online] <https://market.android.com/details?id=book-8Xp4rgEACAAJ> (accessed 24 July 2019).

- Chen, W., Yin, G., Feng, Z. and Liao, X. (2018) 'Effect of powder feedstock on microstructure and mechanical properties of the 316L stainless steel fabricated by selective laser melting', *Metals, Multidisciplinary Digital Publishing Institute*, Vol. 8, No. 9, p.729.
- Chen, W.W. and Song, B. (2010) *Split Hopkinson (Kolsky) Bar: Design, Testing and Applications*, Springer Science & Business Media, New York.
- Cherry, J.A., Davies, H.M., Mehmood, S., Lavery, N.P., Brown, S.G.R. and Sienz, J. (2015) 'Investigation into the effect of process parameters on microstructural and physical properties of 316L stainless steel parts by selective laser melting', *International Journal of Advanced Manufacturing Technology*, Vol. 76, No. 5, pp.869–879.
- Cilas (2018) *Particle Size Analyzers* [online] http://www.particle-size.com/cilas_1180_particle.htm (accessed 2018).
- Conner, B.P., Manogharan, G.P., Martof, A.N., Rodomsky, L.M., Rodomsky, C.M., Jordan, D.C. and Limperos, J.W. (2014) 'Making sense of 3-D printing: creating a map of additive manufacturing products and services', *Additive Manufacturing*, Vols. 1–4, pp.64–76.
- Database, S. (2016) *Materials Results*, 2 May [online] http://senvol.com/5_material-results/ (accessed 24 July 2019).
- Davies, C.M., Withnell, O., Ronnerberg, T., Williams, R. and Hooper, P.A. (2018) 'Fracture analysis of 316L steel samples manufactured by selective laser melting', *Procedia Structural Integrity*, Vol. 13, pp.1384–1389.
- Farayibi, P.K. and Abioye, T.E. (2019) 'Additive manufacture of TiB₂/Ti-6Al-4V metal matrix composite by selective laser melting', *International Journal of Rapid Manufacturing*, Vol. 8, No. 3, pp. 259–270, Inderscience Publishers.
- Ganesh, P., Kaul, R., Sasikala, G., Kumar, H., Venugopal, S., Tiwari, P., Rai, S. et al. (2014) 'Fatigue crack propagation and fracture toughness of laser rapid manufactured structures of AISI 316L stainless steel', *Metallography, Microstructure, and Analysis*, Vol. 3, No. 1, pp.36–45.
- Gong, H., Gu, H., Zeng, K., Dilip, J.J.S., Pal, D., Stucker, B., Christiansen, D. et al. (2014) 'Melt pool characterization for selective laser melting of Ti-6Al-4V pre-alloyed powder', *Proceedings of the Annual Solid Freeform Fabrication Symposium, presented at the Solid Freeform Fabrication Symposium*, pp.256–267.
- Gray III, G.T., Livescu, V., Rigg, P.A., Trujillo, C.P., Cady, C.M., Chen, S.R., Carpenter, J.S. et al. (2015) 'Structure/property (constitutive and dynamic strength/damage) characterization of additively manufactured 316L SS', *EPJ Web of Conferences*, Vol. 94, p.02006, EDP Sciences.
- Gray, G.T., Livescu, V., Rigg, P.A., Trujillo, C.P., Cady, C.M., Chen, S.R., Carpenter, J.S. et al. (2017) 'Structure/property (constitutive and spallation response) of additively manufactured 316L stainless steel', *Acta Materialia*, Vol. 138, pp.140–149.
- Gu, D. (2015) *Laser Additive Manufacturing of High-Performance Materials*, Springer-Verlag Berlin Heidelberg, Berlin, Germany.
- ISO/ASTM (2015) *Standard Terminology for Additive Manufacturing – General Principles – Terminology*, No. 52900-15, ASTM International, West Conshohocken, PA.
- Johnson, A.A., Bingham, G.A. and Majewski, C.E. (2015) 'Laser sintered body armour: establishing guidelines for dual-layered stab protection', *International Journal of Rapid Manufacturing*, Vol. 5, No. 1, pp.3–19.
- Keicher, D.M., Romero, J.A., Atwood, C.L., Griffith, M.L., Jeantette, F.P., Harwell, L.D., Greene, D.L. et al. (1996) *Free Form Fabrication Using the Laser Engineered Net Shaping (LENS[®])*, Process, Sandia National Laboratories (SNL), <https://doi.org/10.2172/425303>.
- Kempen, K., Yasa, E., Thijs, L., Kruth, J.-P. and Van Humbeeck, J. (2011) 'Microstructure and mechanical properties of Selective Laser Melted 18Ni-300 steel', *Physics Procedia*, Vol. 12, pp.255–263.

- Khan, M. and Dickens, P. (2014) 'Selective laser melting (SLM) of pure gold for manufacturing dental crowns', *Rapid Prototyping Journal*, Emerald Group Publishing Limited, <https://doi.org/10.1108/RPJ-03-2013-0034>.
- Kong, D., Ni, X., Dong, C., Zhang, L., Man, C., Cheng, X. and Li, X. (2019) 'Anisotropy in the microstructure and mechanical property for the bulk and porous 316L stainless steel fabricated via selective laser melting', *Materials Letters*, Vol. 235, pp.1–5.
- Król, M., Dobrzański, L. and Reimann, I.C. (2013) 'Surface quality in selective laser melting of metal powders', *Archives of Materials Science*, Vol. 60, No. 2, pp.87–92.
- Kruth, J.P., Froyen, L., Van Vaerenbergh, J., Mercelis, P., Rombouts, M. and Lauwers, B. (2004) 'Selective laser melting of iron-based powder', *Journal of Materials Processing Technology*, Vol. 149, No. 1, pp.616–622.
- Lee, W-S. and Chiu, C-C. (2006) 'Deformation and fracture behavior of 316L sintered stainless steel under various strain rate and relative sintered density conditions', *Metallurgical and Materials Transactions A*, Vol. 37, No. 12, pp.3685–3696.
- Lee, W-S., Lin, C-F. and Liu, T-J. (2006) 'Strain rate dependence of impact properties of sintered 316L stainless steel', *Journal of Nuclear Materials*, Vol. 359, No. 3, pp.247–257.
- Lee, W-S., Lin, C-F., Chen, T-H. and Luo, W-Z. (2012) 'High temperature deformation and fracture behaviour of 316L stainless steel under high strain rate loading', *Journal of Nuclear Materials*, Vol. 420, No. 1, pp.226–234.
- Li, R., Shi, Y., Wang, Z., Wang, L., Liu, J. and Jiang, W. (2010) 'Densification behavior of gas and water atomized 316L stainless steel powder during selective laser melting', *Applied Surface Science*, Vol. 256, No. 13, pp.4350–4356.
- Lou, X., Andresen, P.L. and Rebak, R.B. (2018) 'Oxide inclusions in laser additive manufactured stainless steel and their effects on impact toughness and stress corrosion cracking behavior', *Journal of Nuclear Materials*, Vol. 499, pp.182–190.
- Ma, M., Wang, Z., Gao, M. and Zeng, X. (2015) 'Layer thickness dependence of performance in high-power selective laser melting of 1Cr18Ni9Ti stainless steel', *Journal of Materials Processing Technology*, Vol. 215, pp.142–150.
- Majumdar, J.D., Pinkerton, A., Liu, Z., Manna, I. and Li, L. (2005) 'Microstructure characterisation and process optimization of laser assisted rapid fabrication of 316L stainless steel', *Applied Surface Science*, Vol. 247, No. 1, pp.320–327.
- Manogharan, G., Conner, B., Sirichakwal, I., Strong, D., Wakefield, T. and Kay, M. (2018) 'Adopting additive-hybrid manufacturing: the role of capacity in implementation decision', *International Journal of Rapid Manufacturing*, Vol. 7, No. 4, p.337.
- Mindt, H-W., Megahed, M., Lavery, N.P., Giordimaina, A. and Brown, S.G.R. (2016) 'Verification of numerically calculated cooling rates of powder bed additive manufacturing', in The Minerals, Metals & Materials Society (Ed.): *TMS 2016 145th Annual Meeting & Exhibition*, Vol. 39, pp.205–212, Springer International Publishing, Cham.
- Montero Sistiaga, M., Nardone, S., Hautfenne, C. and Van Humbeeck, J. (2016) 'Effect of heat treatment of 316L stainless steel produced by selective laser melting (SLM)', *Proceedings of the 27th Annual International Solid Freeform Fabrication Symposium-An Additive Manufacturing Conference*, pp.558–565.
- Monzon, Ortega, Z., Martinez, A. and Ortega, F. (2015) 'Standardization in additive manufacturing: activities carried out by international organizations and projects', *International Journal of Advanced Manufacturing Technology*, Vol. 76, Nos. 5-8, pp.1111–1121.
- Qiu, C., Adkins, N.J.E. and Attallah, M.M. (2013) 'Microstructure and tensile properties of selectively laser-melted and of HIPed laser-melted Ti–6Al–4V', *Materials Science and Engineering: A*, Vol. 578, pp.230–239.
- Qiu, C., Panwisawas, C., Ward, M., Basoalto, H.C., Brooks, J.W. and Attallah, M.M. (2015) 'On the role of melt flow into the surface structure and porosity development during selective laser melting', *Acta Materialia*, Vol. 96, pp.72–79.

- Riemer, A., Leuders, S., Thöne, M., Richard, H.A., Tröster, T. and Niendorf, T. (2014) 'On the fatigue crack growth behavior in 316L stainless steel manufactured by selective laser melting', *Engineering Fracture Mechanics*, Vol. 120, pp.15–25.
- Romano, S., Brückner-Foit, A., Brandão, A., Gumpinger, J., Ghidini, T. and Beretta, S. (2017) 'Fatigue properties of AlSi10Mg obtained by additive manufacturing: defect-based modelling and prediction of fatigue strength', *Engineering Fracture Mechanics*, <https://doi.org/10.1016/j.engfracmech.2017.11.002>.
- Rombouts, M., Kruth, J.P., Froyen, L. and Mercelis, P. (2006) 'Fundamentals of selective laser melting of alloyed steel powders', *CIRP Annals*, Vol. 55, No. 1, pp.187–192.
- Santos, E.C., Osakada, K., Shiomi, M., Kitamura, Y. and Abe, F. (2004) 'Microstructure and mechanical properties of pure titanium models fabricated by selective laser melting', *Proceedings of the Institution of Mechanical Engineers, Part C: Journal of Mechanical Engineering Science, IMECHE*, Vol. 218, No. 7, pp.711–719.
- Simchi, A. (2006) 'Direct laser sintering of metal powders: mechanism, kinetics and microstructural features', *Materials Science and Engineering: A*, Vol. 428, No. 1, pp.148–158.
- Simchi, A., Petzoldt, F. and Pohl, H. (2003) 'On the development of direct metal laser sintering for rapid tooling', *Journal of Materials Processing Technology*, Vol. 141, No. 3, pp.319–328.
- Simonelli, M., Tse, Y.Y. and Tuck, C. (2014) 'On the texture formation of selective laser melted Ti-6Al-4V', *Metallurgical and Materials Transactions A*, Vol. 45, No. 6, pp.2863–2872.
- Spierings, A.B. and Levy, G. (2009) 'Comparison of density of stainless steel 316L parts produced with selective laser melting using different powder grades', *Proceedings of the Annual International Solid Freeform Fabrication Symposium*, presented at the *International Solid Freeform Fabrication Symposium*, pp.342–353.
- Stwora, A. and Skrabalak, G. (2013) 'Influence of selected parameters of Selective Laser Sintering process on properties of sintered materials', *Journal of Achievements in Materials and Manufacturing Engineering*, Vol. 61, No. 2, pp.375–380.
- Tang, P., Xie, H., Wang, S., Ding, X., Zhang, Q., Ma, H., Yang, J. et al. (2019) 'Numerical analysis of molten pool behavior and spatter formation with evaporation during selective laser melting of 316L stainless steel', *Metallurgical and Materials Transactions B*, <https://doi.org/10.1007/s11663-019-01641-w>.
- Tolosa, I., Garcandía, F., Zubiri, F., Zapirain, F. and Esnaola, A. (2010) 'Study of mechanical properties of AISI 316 stainless steel processed by 'selective laser melting', following different manufacturing strategies', *International Journal of Advanced Manufacturing Technology*, Vol. 51, No. 5, pp.639–647.
- Trelewicz, J.R., Halada, G.P., Donaldson, O.K. and Manogharan, G. (2016) 'Microstructure and corrosion resistance of laser additively manufactured 316L stainless steel', *JOM Journal of the Minerals Metals and Materials Society*, Vol. 68 No. 3, pp.850–859, Springer US.
- Tsopanos, S., Mines, R.A.W., McKown, S., Shen, Y., Cantwell, W.J., Brooks, W. and Sutcliffe, C.J. (2010) 'The influence of processing parameters on the mechanical properties of selectively laser melted stainless steel microlattice structures', *Journal of Manufacturing Science and Engineering, American Society of Mechanical Engineers*, Vol. 132, No. 4, p.041011.
- Vrancken, B., Cain, V., Knutsen, R. and Van Humbeeck, J. (2014a) 'Residual stress via the contour method in compact tension specimens produced via selective laser melting', *Scripta Materialia*, Vol. 87, pp.29–32.
- Vrancken, B., Thijs, L.-P., Kruth, J. and Van Humbeeck, J. (2014b) 'Microstructure and mechanical properties of a novel β titanium metallic composite by selective laser melting', *Acta Materialia*, Vol. 68, pp.150–158.
- Winter, R.E., Cotton, M., Harris, E.J., Maw, J.R., Chapman, D.J., Eakins, D.E. and McShane, G. (2014) 'Plate-impact loading of cellular structures formed by selective laser melting', *Modelling and Simulation in Materials Science and Engineering*, Vol. 22, No. 2, p.025021, IOP Publishing.

- Yadroitsev, I. and Smurov, I. (2010) 'Selective laser melting technology: from the single laser melted track stability to 3D parts of complex shape', *Physics Procedia*, Vol. 5, pp.551–560.
- Yadroitsev, I. and Smurov, I. (2011) 'Surface morphology in selective laser melting of metal powders', *Physics Procedia*, Vol. 12, pp.264–270.
- Yadroitsev, I., Thivillon, L., Bertrand, P. and Smurov, I. (2007) 'Strategy of manufacturing components with designed internal structure by selective laser melting of metallic powder', *Applied Surface Science*, Vol. 254, No. 4, pp.980–983.
- Yakout, M., Elbestawi, M.A. and Veldhuis, S.C. (2019) 'Density and mechanical properties in selective laser melting of Invar 36 and stainless steel 316L', *Journal of Materials Processing Technology*, Vol. 266, pp.397–420.
- Yasa, E. and Kruth, J-P. (2011) 'Microstructural investigation of selective laser melting 316L stainless steel parts exposed to laser re-melting', *Procedia Engineering*, Vol. 19, pp.389–395.
- Zhou, L., Mehta, A., Schulz, E., McWilliams, B., Cho, K. and Sohn, Y. (2018) 'Microstructure, precipitates and hardness of selectively laser melted AlSi10Mg alloy before and after heat treatment', *Materials Characterization*, Vol. 143, pp.5–17.
- Zhou, X., Li, K., Zhang, D., Liu, X., Ma, J., Liu, W. and Shen, Z. (2015) 'Textures formed in a CoCrMo alloy by selective laser melting', *Journal of Alloys and Compounds*, Vol. 631, pp.153–164.